Journal of Materials Chemistry C

ROYAL SOCIETY OF CHEMISTRY

PAPER

View Article Online
View Journal

Cite this: DOI: 10.1039/d4tc04026k

Electrochemically controllable emission and coloration using a modified electrode with a layered clay compound containing viologen derivative and europium(III) complex†

Rong Cao, Naoto Kobayashi, Kazuki Nakamura * and Norihisa Kobayashi *

Novel displays based on electrochemical reactions have significant potential for various applications. In this study, a layered clay compound was used to immobilize a luminescent Eu(III) complex and an electrochromic viologen derivative (heptylviologen, HV^{2+}) on an electrode to construct a novel dual-mode display device capable of achieving electro-switchable emission and coloration. X-ray powder diffraction, absorption, photoluminescence, cyclic voltammograms, and luminescence lifetimes were recorded to elucidate the structure and photoelectrochemical properties of the hybrid clay material containing the Eu(III) complex and HV^{2+}. The electrochromic HV^{2+} and Eu(III) complex were adsorbed on/between the clay layers, and it was found that approximately 80% of HV^{2+} and 20% of Eu(III) complex were adsorbed in cases with a 25%:16.7% *vs.* cation exchange capacity (CEC) ratio. The insertion of the Eu(III) complex resulted in the expansion of the interlayer spacing, facilitating the movements of the supporting electrolyte between the layers and improving the electrochemical redox reaction of HV^{2+}. By constructing a two-electrode device using a hybrid clay-modified electrode, the coloration and emission of the device were electrochemically modulated through the redox reaction of HV^{2+}. The dual-mode representation was achieved *via* excitation energy transfer from the Eu(III) complex to the colored $HV^{\bullet+}$ and the reabsorption of the luminescence from the Eu(III) complex. This modulation of the electrochemical properties of layered clay compounds holds potential for the development of advanced electrochemical systems and innovative display devices.

Received 20th September 2024,
Accepted 14th November 2024

DOI: 10.1039/d4tc04026k

rsc.li/materials-c

1 Introduction

In recent years, stimuli-responsive materials that exhibit changes in their photophysical properties in response to external stimuli have attracted extensive research interest because of their wide-ranging applications in chemical sensors,[1] biomedicine,[2] molecular logic gates,[3] molecular memories,[4] and display devices.[5] The photophysical properties of these materials can be manipulated *via* specific external triggers, such as thermal,[6–8] electrical,[9] optical[10] or chemical stimuli,[11–13] enabling the reversible switching of optical properties in materials with thermosensitive, electroactive, photoactive, or pH-sensitive functions.

Among the various external stimuli, we focused on electrochemical stimuli-responsive materials because electrical stimuli can be rapidly and repeatedly applied to display devices. Electrochromic (EC) molecules undergo color changes *via* electrochemical redox reactions at a low voltage.[14,15] Therefore, they are potential candidates for functional devices, such as smart windows,[16–18] digital signage,[19] and e-paper displays.[20] In addition to coloration control, emission modulation is also important because of its impact on various applications. Within this category, the electrofluorochromic (EFC) technology stands out for its potential in the development of multifunctional electrochromic devices, as it enables the achievement of multi-mode display devices *via* electrochemical redox reactions.[21,22] Electrofluorochromism arises from the unique properties of photoelectrochemical functional materials that allow the reversible modulation of photoluminescence under an applied electric potential.[22–24] Consequently, the integration of the EC and EFC technologies has emerged as a promising approach for the development of advanced multifunctional displays.[25]

We previously reported a pioneering work on the integration of EC [viologen derivatives (HV^{2+})] and EFC materials [Eu(III) complex] to fabricate a dual-mode display (DMD) device. The

Graduate School of Engineering, Chiba University, 1-33, Yayoi-cho, Inage-ku, Chiba, 263-8522, Japan. E-mail: Nakamura.Kazuki@faculty.chiba-u.jp, koban@faculty.chiba-u.jp; Fax: +81-43-290-3458; Tel: +81-43-290-3457

† Electronic supplementary information (ESI) available. See DOI: https://doi.org/10.1039/d4tc04026k

DMD device synchronously controls both emission and coloration *via* electrochemical redox reactions.[26] Fluorescence switching is induced by the transfer of excitation energy from a luminescent material to an electrochemically active material in response to electrical stimuli.[27] Since then, the development of display devices using integrated EC and EFC materials has been a focus of research.[28–30] HV^{2+}, a typical electrochemically active material, exhibits reversible oxidation and reduction at low potentials to form stable free radical cations, accompanied by strong electrochromism, changing the color of the transparent solution to a deep blue.[31] Eu(III) complexes are known for their unique optical properties, such as high luminescence purity, long luminescence lifetime, high transparency in the visible light region, and large pseudo-Stokes shifts, resulting in their wide-range applications, especially in phosphors, biological images, and probes.[32–36]

In the electrochemical systems, integrating functional materials onto the electrode surface rather than dispersing them in solution enhances the electrochemical performance, leading to faster response times, higher reaction efficiencies, and long-term stability of electrochemical devices.[37] Layered clay compounds can be used for the integration of these functional materials owing to their distinctive properties such as strong adsorption and high ion exchange capacity.[38–41] As shown in Fig. 1a, smectite is a 2 : 1-type clay with two silicon–oxygen tetrahedral layers and an aluminum–oxygen octahedral layer, which provides a unique environment for chemical reactions. Although clay has a low electrical conductivity, it can still demonstrate electrochemical activity after being combined with electrochemically active materials. Therefore, the introduction of electrochemically active materials into clays as electrode materials has become an important research topic.[42–44] On the other hand, clay-based luminescent hybrid materials have attracted significant interest because they not only retain their excellent luminescent properties but also improve the poor stability of lanthanide complexes.[45–47] However, strategies for developing EFC multifunctional materials and devices based on clay compounds have been rare, especially in the exploration of EC/EFC multifunctional materials and devices.

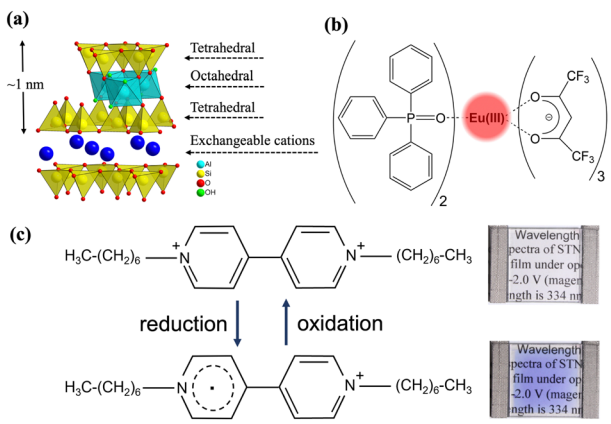

Fig. 1 Chemical structure of (a) smectite, (b) $Eu(hfa)_3(TPPO)_2$, and (c) HV^{2+}.

In this study, we used a clay compound of smectite and prepared a novel electrochemical DMD device by employing an Eu(III) complex as a luminescent molecule and heptyl viologen (HV^{2+}) as an electrochromic molecule in the smectite matrix (the chemical structures of these molecules are shown in Fig. 1). The working electrode modified with the clay/HV^{2+}/Eu(III) complex film was prepared, and the photophysical properties and electrochemical properties of the multifunctional hybrid material were studied in detail. Successful coloration and emission control were achieved *via* electrochemical reactions alone.

2 Experimental section

2.1 Materials

All the chemicals were commercially available and used as received without further purification. Europium(III) acetate *n*-hydrate (99.9%), hexafluoroacetylacetone (hfa-H_2), triphenylphosphine oxide (TPPO) and the electrochromic molecule 1,1′-diheptyl-4,4′-bipyridinium dibromide (HV^{2+}) compound were purchased from Tokyo Chemical Industry Co., Ltd, Tokyo, Japan. Smectite (Sumecton STN) with a CEC of 60 meq/100 g was purchased from Kunimine Industries Co., Ltd, Tokyo, Japan. The chemical formula of STN is $[(C_8H_{17})_3(CH_3)N]_{0.33}[(Mg_{2.67}Li_{0.33})Si_4O_{10}(OH)_2]$. Methyltri-*n*-octylammonium ions $[(C_8H_{17})_3(CH_3)N]_{0.33}$ are intercalated between the layers of smectite, resulting in its uniform dispersion in medium-to-high polar solvents. The plastic spacers were purchased from Lintec Corporation, Tokyo, Japan. Propylene carbonate (PC), acetonitrile, and tetra-*n*-butylammonium perchlorate (TBAP) were purchased from KANTO Chemical Co., Inc., Tokyo, Japan. The $Eu(hfa)_3(TPPO)_2$ complex, synthesized according to a previously reported procedure,[48] was used in this study.

2.2 Preparation of the EC electrolyte

STN solutions were prepared by dispersing 1 wt% STN in acetonitrile. For the STN/HV^{2+} hybrid solution, STN (1 wt%) and HV^{2+} (1.2 mmol L^{-1}) were dispersed and dissolved in acetonitrile with a 25% *vs.* CEC ratio. Similarly, the STN/$Eu(hfa)_3(TPPO)_2$ hybrid solution was prepared by dispersing STN (1 wt%) and $Eu(hfa)_3(TPPO)_2$ (0.8 mmol L^{-1}) in acetonitrile with a 16.7% *vs.* CEC ratio. The STN/HV^{2+}/$Eu(hfa)_3(TPPO)_2$ hybrid solution (1 wt%, 1.2 mmol L^{-1}, and 0.8 mmol L^{-1}, respectively) was prepared in acetonitrile for a 25% : 16.7% *vs.* CEC ratio. The concentrations of HV^{2+} range from 0.24 mmol L^{-1} to 1.2 mmol L^{-1}, while the concentrations of $Eu(hfa)_3(TPPO)_2$ range from 0.16 mmol L^{-1} to 0.8 mmol L^{-1} in a clay-dispersed solution. The molar ratios of HV^{2+} and $Eu(hfa)_3(TPPO)_2$ molecules compared to the amount of cation exchange of STN from 5% : 3.3% *vs.* CEC to 25% : 16.7% *vs.* CEC. The supporting electrolyte solution was prepared by dissolving 200 mmol L^{-1} TBAP in PC solvent. All solutions were prepared at room temperature.

2.3 Fabrication of the EC device

First, the surface of the ITO electrode was cleaned and treated with UV/O_3 for 20 min. Subsequently, 0.2 mL of the STN/HV^{2+}

solution, STN/Eu(hfa)$_3$(TPPO)$_2$ solution, and STN/HV^{2+}/Eu(hfa)$_3$(TPPO)$_2$ dispersion solutions were drop cast onto the ITO electrodes, and the corresponding films were obtained after drying at room temperature. These modified films were used as the working electrodes (active area: 2 cm^2), with a Pt wire as the counter electrode and an Ag/Ag$^+$ electrode as the reference electrode, which were placed into the electrolyte solution.

2.4 Preparation of the 2-electrode device

First, the surface of the ITO electrode was cleaned and treated with UV/O$_3$ for 20 min. Subsequently, 0.2 mL of the STN/HV^{2+} solution, STN/Eu(hfa)$_3$(TPPO)$_2$ solution and STN/HV^{2+}/Eu(hfa)$_3$(TPPO)$_2$ solutions prepared in Section 2.2 were drop-cast onto the center of the plastic spacer on the ITO electrode surface, and the corresponding films were obtained after drying at room temperature. The 2-electrode device was prepared by sandwiching the electrolyte solution between an ITO electrode modified with the STN/HV^{2+}, STN/Eu(hfa)$_3$(TPPO)$_2$, or STN/HV^{2+}/Eu(hfa)$_3$(TPPO)$_2$ film and an unmodified ITO electrode.

2.5 Measurements

Powder X-ray diffraction (PXRD) was performed using an X-ray powder diffractometer (AXS D8 ADVANCE, Bruker AXS, Karlsruhe, Germany) with a Cu Kα radiation source (λ = 1.5418 Å), operating at 40 kV and 40 mA. Ultraviolet-visible (UV-vis) absorption spectra were recorded using a spectrophotometer (V-570, JASCO Inc., Tokyo, Japan) and quartz cells with a 10 mm long optical path were used. Photo-luminescence spectra (PL) were recorded using a spectrofluorometer (FP-6600, JASCO Inc., Tokyo, Japan). The emission lifetimes were determined using a time-resolved fluorescence spectrometer (Quantaurus-Tau C11367-21, Hamamatsu Photonics K. K., Tokyo, Japan). Cyclic voltammetry (CV) experiments and chronoamperometry experiments were performed at a scan rate of 50 mV s^{-1} using a potentiostat/galvanostat (ALS660A; CH Instruments, Inc., Austin, TX, USA) controlled by a computer. The *in situ* absorption spectra of the three- and two-electrode devices were recorded using a fiber-optic spectrometer system (USB2000, Ocean Optics, Orlando, FL, USA) during potential or voltage sweeping.

3 Results and discussion

3.1 Interaction between STN, Eu(hfa)$_3$(TPPO)$_2$ and HV^{2+}

In this study, the intercalation of Eu(hfa)$_3$(TPPO)$_2$ and HV^{2+} into the STN layers was examined using XRD (Fig. 2). The original smectite with metal ions or H$_2$O molecules exhibits the 001 peak at approximately 6.5°.[49] After the intercalation of methyltri-*n*-octylammonium ions, the interlayer spacing increases, causing the 001 peak to shift to 5°.[50,51] The interlayer spacing d of pristine STN was calculated to be approximately 1.72 nm using the Bragg equation ($2d \sin\theta = n\lambda$). Compared with the STN film, the STN/HV^{2+} film exhibited a broader peak at 5° and a shoulder peak at 4.35°, expanding the interlayer spacing to 2.03 nm. The interlayer spacing of the HV^{2+} molecules varied from 0.43 nm to 2.6 nm depending on the direction

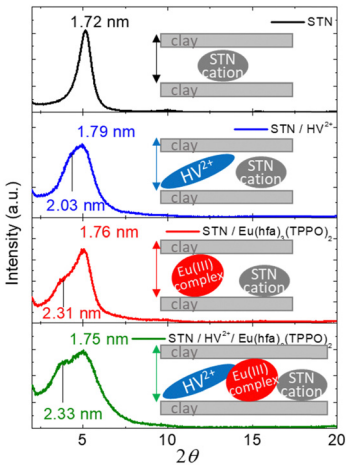

Fig. 2 X-ray diffraction (XRD) patterns of the STN film, STN/HV^{2+} film, STN/Eu(hfa)$_3$(TPPO)$_2$ film, and STN/HV^{2+}/Eu(hfa)$_3$(TPPO)$_2$ film.

of insertion (Fig. S1(a), ESI†), and the thickness of the STN layer was approximately 1 nm.[40] This suggests that HV^{2+} molecules were inserted into the STN layer at a specific angle. Similarly, for the STN/Eu(hfa)$_3$(TPPO)$_2$ film, the shoulder peak shifted to approximately 3.8°, with the interlayer spacing increasing to 2.31 nm. By estimating the size of the Eu(hfa)$_3$(TPPO)$_2$ roughly from the result of single crystal XRD,[52] it has a minimum size of 1.08 nm and a maximum size of 1.6 nm (Fig. S1(b), ESI†). It indicated that the Eu(hfa)$_3$(TPPO)$_2$ molecules are inserted into the STN interlayers. The STN/HV^{2+}/Eu(hfa)$_3$(TPPO)$_2$ film showed the presence of both HV^{2+} and Eu(hfa)$_3$(TPPO)$_2$ due to the broad peak at 5° and the shoulder peak around 3.8°, which indicates the intercalation of HV^{2+} and Eu(hfa)$_3$(TPPO)$_2$ into the STN layers. Even after the insertion of the Eu(hfa)$_3$(TPPO)$_2$ complex and HV^{2+} molecules, the peak around 5° (1.7 nm) in the XRD patterns remains, indicating that the Eu(hfa)$_3$(TPPO)$_2$ complex and HV^{2+} molecules are inserted into part of the STN interlayers, while other STN layers remain unintercalated.

The UV-vis absorption spectra of the hybrid material solutions were recorded between 200 and 700 nm. As shown in Fig. S2(a) (ESI†), an absorption peak was observed at approximately 260 nm for the HV^{2+} molecule. Interestingly, after the addition of STN (blue line in Fig. S2(a) (ESI†) and Fig. 3), a new absorption peak appeared near 400 nm (inset of Fig. 3). As shown in Fig. S3 (ESI†), the emission spectra of HV^{2+}, STN/HV^{2+}, and STN/HV^{2+}/Eu(hfa)$_3$(TPPO)$_2$ were measured with an excitation wavelength of 260 nm. It was observed that only STN/HV^{2+} solution exhibited an emission peak around 520 nm. Under the UV irradiation, the STN/HV^{2+} solution emitted green fluorescence. We speculate that the new absorption peak at 400 nm is related to the new emission peak at 520 nm. The HV^{2+} molecule is inserted into the interlayer, and some interactions such as fixation, aggregation or charge transfer occur between STN and HV^{2+} molecules within the confined interlayer space. These interactions result in the observed green fluorescence and the appearance of a new absorption peak at

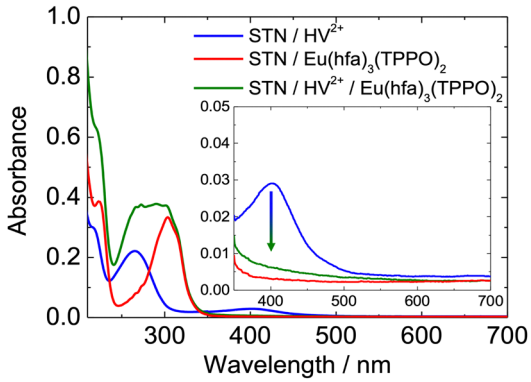

Fig. 3 Absorption spectra of STN/HV^{2+} solution, STN/$Eu(hfa)_3(TPPO)_2$ solution, and STN/HV^{2+}/$Eu(hfa)_3(TPPO)_2$ solution. Inset: Enlarged view of the absorption spectrum in the range of 350 nm to 700 nm.

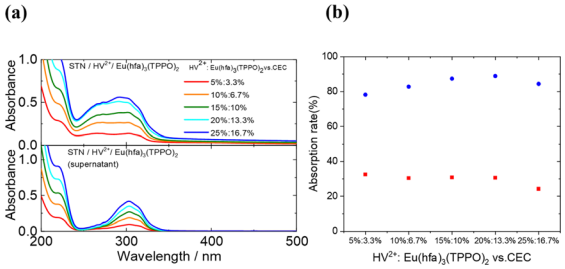

Fig. 4 (a) Absorption spectra of different ratios of STN/HV^{2+}/$Eu(hfa)_3(TPPO)_2$ hybrid solutions (top) and supernatants (bottom); (b) adsorption ratios of HV^{2+} (blue dots) and $Eu(hfa)_3(TPPO)_2$ (red dots) at different ratios.

400 nm.[53,54] The interactions will be explored in our future studies. Following this, the absorption properties of the $Eu(hfa)_3(TPPO)_2$ were investigated. As shown in Fig. S2(b) (ESI†), the absorption peak of $Eu(hfa)_3(TPPO)_2$ at approximately 300 nm, remained unchanged after adding STN.

As shown in Fig. 3, for the STN/HV^{2+}/$Eu(hfa)_3(TPPO)_2$ solution, the peak near 290 nm broadened because of the overlapping of the absorption peaks of the HV^{2+} (around 260 nm) and the $Eu(hfa)_3(TPPO)_2$ (around 300 nm) in smectite solution. However, the absorption peak around 400 nm for the HV^{2+} molecules and green fluorescence of hybrid solution disappeared after the addition of the $Eu(hfa)_3(TPPO)_2$ complex (Fig. S3, ESI†). The insertion of $Eu(hfa)_3(TPPO)_2$ into the STN layers increased the interlayer spacing, which weakened or eliminated the interactions. This observation is consistent with the XRD results shown in Fig. 2. Overall, these results suggest the coexistence of HV^{2+} and $Eu(hfa)_3(TPPO)_2$ in the same STN layers.

To evaluate the adsorption capacity of HV^{2+} and $Eu(hfa)_3(TPPO)_2$ on the STN, the absorption spectra of the STN/HV^{2+}/$Eu(hfa)_3(TPPO)_2$ hybrid solutions and supernatants after centrifugation were measured. For the STN/HV^{2+} and STN/$Eu(hfa)_3(TPPO)_2$ solutions respectively, Fig. S4 and S5 (ESI†) showed a significant decrease in the absorbance of the supernatant solutions after centrifugation, indicating that HV^{2+} and $Eu(hfa)_3(TPPO)_2$ were intercalated between the STN layers and removed by centrifugation. Based on the absorbance measurements, the adsorption ratios of HV^{2+} and $Eu(hfa)_3(TPPO)_2$ were approximately 80% and 35%, respectively. Fig. 4(a) shows that the absorption peak of HV^{2+} near 270 nm is significantly reduced after centrifugation, whereas that of $Eu(hfa)_3(TPPO)_2$ near 300 nm exhibits a smaller decrease than that for HV^{2+}. This indicates that HV^{2+} is more easily adsorbed by the STN matrix owing to the negative charges of the STN layers, which favors the adsorption of cationic species such as HV^{2+}. $Eu(hfa)_3(TPPO)_2$ adsorbed on STN *via* hydrophobic interaction of methyltri-*n*-octylammonium ions, which have hydrophobic long alkyl chains. Although van der Waals forces are relatively weak, they also contribute to intermolecular interactions and play an auxiliary role in the adsorption process.[47] Additionally, we have previously reported on the interaction between non-ionic Eu(III) complexes and these types of alkyl ammonium cations in solution, solid-state, and polymer matrices such as DNA-CTMA.[55,56] Compared with the STN/$Eu(hfa)_3(TPPO)_2$ solution without HV^{2+} (Fig. S5, ESI†), the adsorption percentage of $Eu(hfa)_3(TPPO)_2$ in the STN/HV^{2+}/$Eu(hfa)_3(TPPO)_2$ hybrid solution was higher under lower CEC conditions. This was attributed to HV^{2+} expanding the STN interlayer spacing of the STN matrix, thereby facilitating the adsorption of the Eu(III) complex.

When estimating the adsorption ratios, Fig. 4(b) shows that approximately 80% of HV^{2+} and about 20% of $Eu(hfa)_3(TPPO)_2$ are adsorbed in cases with a 25%:16.7% *vs.* CEC ratio. Therefore, 50% of the anionic sites of STN were occupied by $Eu(hfa)_3(TPPO)_2$ and HV^{2+}, and the remaining 50% were occupied by the original methyltri-*n*-octylammonium ion cations. This suggests that parts of the STN do not undergo molecular insertion.

In addition, as shown in Fig. S6 (ESI†), the emission spectra and time-resolved emission decay curves of $Eu(hfa)_3(TPPO)_2$, STN/$Eu(hfa)_3(TPPO)_2$, and STN/HV^{2+}/$Eu(hfa)_3(TPPO)_2$ solutions indicate that the Eu(III) complex exists in a stable molecular form in these hybrid solutions without dissociation.[57] This is evidenced by the unchanged number and position of the emission transitions for Eu^{3+} ($^5D_0 \rightarrow {}^7F_J$, J = 0, 1, 2, 3, 4), and the emission transition of $^5D_0 \rightarrow {}^7F_0$ shows only one peak, suggesting a single predominant chemical environment surrounding the Eu(III) ions (Fig. S6(a), ESI†).[58] Additionally, as shown in Fig. S6(b) (ESI†), all solutions exhibit emission decay curves with only one exponential component ($\sim$0.84 ms). This mono-exponential emission decay is attributed to the presence of a single emitting species of the Eu(III) complex.[59]

3.2 Electrochromic properties of modified electrodes

To investigate the electrochemical properties of the STN/HV^{2+} film, STN/$Eu(hfa)_3(TPPO)_2$ film, and STN/HV^{2+}/$Eu(hfa)_3(TPPO)_2$ film modified on ITO electrodes, CVs and *in situ* absorbance changes at 610 nm were recorded. As shown in Fig. 5(a), the STN/$Eu(hfa)_3(TPPO)_2$-based electrode does not exhibit any evident reduction or oxidation reactions within the measured potential range. However, the reductive current of the

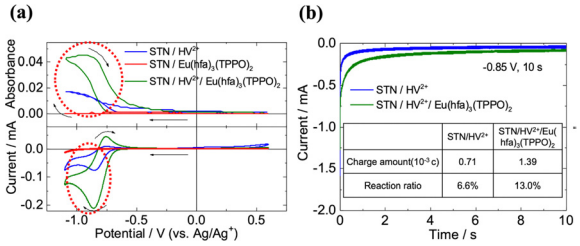

Fig. 5 (a) Change in absorbance at 610 nm (top) and cyclic voltammograms (bottom) of STN/HV^{2+}, STN/$Eu(hfa)_3(TPPO)_2$, and STN/HV^{2+}/$Eu(hfa)_3(TPPO)_2$; (b) chronoamperometric curves of the STN/HV^{2+} film (blue line) and STN/HV^{2+}/$Eu(hfa)_3(TPPO)_2$ film (green line). The inserted table shows the reaction charge amount and reaction ratio of HV^{2+} molecule in the sample.

STN/HV^{2+} film-modified electrode increased at 610 nm during the potential sweep in the negative direction, which is attributed to the typical EC reaction of HV^{2+}.[60] This indicates that even when HV^{2+} is intercalated into the STN matrix, which is originally an insulator, redox hopping can still occur, resulting in redox reactions.[61] For the STN/HV^{2+}/$Eu(hfa)_3(TPPO)_2$ film-modified electrode, the reduction current and the absorbance around −0.7 V almost doubled compared with the STN/HV^{2+} film-modified electrode. This enhancement was attributed to the insertion of the $Eu(hfa)_3(TPPO)_2$ complex, which increased the interlayer distance of the STN matrix, as shown in XRD results shown in Fig. 2, thereby allowing more supporting electrolytes to enter the interlayer space, thus enhancing the redox reaction of HV^{2+}. Fig. 5(b) presents the chronoamperometric results obtained using the STN/HV^{2+} film and STN/HV^{2+}/$Eu(hfa)_3(TPPO)_2$ films as the working electrodes; the inset table displays the reaction charge quantities and reaction ratio of the HV^{2+} molecules in the films. The reaction charge quantities were calculated to be 0.71×10^{-3} C for the STN/HV^{2+} film and 1.39×10^{-3} C for the STN/HV^{2+}/$Eu(hfa)_3(TPPO)_2$ film from the integration of current values.

The quantity of HV^{2+} in the film was determined by calculating the concentration and volume of HV^{2+} in the hybrid solution used for film preparation (0.2 mL, 1.2 mmol L^{-1}). The amount of HV^{2+} in the reaction area was 1.1×10^{-7} mol. By multiplying this value by the Faraday constant (96 485 C mol^{-1}), the charge required for the first reduction of all HV^{2+} molecules in the reactive area was calculated to be 0.011 C. Consequently, the actual reaction ratios for each film were determined using eqn (1).

$$\text{Reaction ratio} = \frac{\text{Actual reaction charge(C)}}{0.011\ \text{C}} \times 100\% \quad (1)$$

As a result, the reaction ratio of HV^{2+} increased from 6.6% to 13.0% owing to the co-existence of $Eu(hfa)_3(TPPO)_2$. This suggests that the inclusion of $Eu(hfa)_3(TPPO)_2$ nearly doubles the reduction reaction ratio of HV^{2+}, which is attributed to $Eu(hfa)_3(TPPO)_2$ expanding the interlayer spacing of the STN matrix, thereby facilitating electron movement and consequently enhancing the reaction ratio of HV^{2+} as indicated by CV measurements.

3.3 Electrochemical modulation of coloration and emission

The two-electrode electrochemical devices were fabricated to demonstrate the simultaneous control of both emission and coloration using the EC reaction of HV^{2+}. First, we considered the EC properties of the two-electrode device prepared using the STN/HV^{2+} film without the Eu(III) complex as the modified electrode (Fig. S7, ESI†). Before applying a bias voltage to the device, no absorption band was observed in the visible region (400–700 nm) (black line in Fig. S7, ESI†). After applying the bias voltage (−2.0 V for 150 s), an absorption band corresponding to the reduced species of $HV^{\bullet+}$ appeared around 610 nm (blue line, Fig. S7, ESI†), resulting in a clear cyan color.

The optical modulation of a two-electrode EFC device containing HV^{2+} and the $Eu(hfa)_3(TPPO)_2$ in a clay matrix was evaluated. As shown in Fig. 6(a), the STN/HV^{2+}/$Eu(hfa)_3(TPPO)_2$-based device exhibits no absorption between 400 nm and 700 nm when no bias voltage is applied (black line), indicating that it has a colorless and transparent appearance, which can be regarded as a "reflection-off" state (photo in Fig. 6(a)).

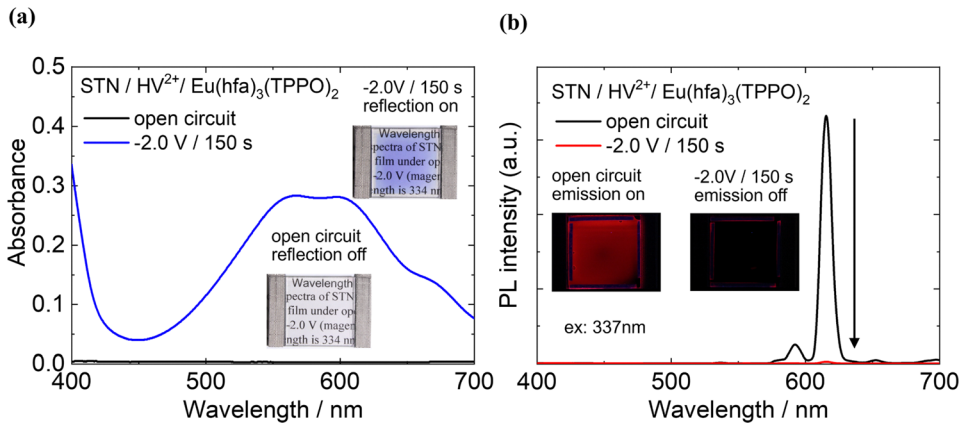

Fig. 6 (a) Absorption spectra of the STN/HV^{2+}/$Eu(hfa)_3(TPPO)_2$ film under open circuit condition (black line) and applied −2.0 V for 150 s (blue line). (b) Emission spectra of the STN/HV^{2+}/$Eu(hfa)_3(TPPO)_2$ film under open circuit condition (black line) and applied −2.0 V for 150 s (red line). Excitation wavelength is 337 nm.

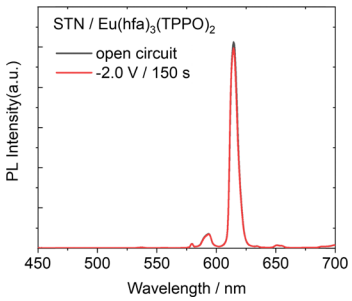

Fig. 7 Emission spectra of STN/Eu(hfa)$_3$(TPPO)$_2$ in the two electrodes device (black line: open circuit condition, red line: under bias voltage of −2 V for 150 s). Excitation wavelength was 337 nm.

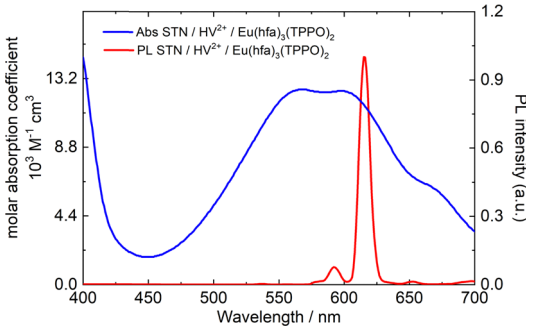

Fig. 9 Absorption spectra under the application of −2.0 V for 150 s (blue line) and normalized emission spectra of Eu(hfa)$_3$(TPPO)$_2$ (red line) under open circuit.

When a bias voltage of −2.0 V was applied for 150 s, new absorption bands appeared near 400 nm and 600 nm, which can be assigned to the reduced species of HV^+ and HV. In our previous report, the absorbance around 337 nm showed almost no change after the reduction of the HV^{2+} molecule.[27] Therefore, the reduced species of HV^+ and HV has a minimal impact on the absorption of the excitation light for the Eu(III) complex. As the intensity of the new absorption bands increased, the color of the device changed from colorless to cyan, representing the "reflection-on" state. Compared with the STN/HV^{2+}-based device without Eu(hfa)$_3$(TPPO)$_2$ (Fig. S7, ESI†), the absorbance at 600 nm of the STN/HV^{2+}/Eu(hfa)$_3$(TPPO)$_2$-based device significantly increased. This is consistent with the results shown in Fig. 5, wherein an increased reduction reaction ratio of HV^{2+} was observed after the addition of Eu(hfa)$_3$(TPPO)$_2$.

The photoluminescence properties of the device under redox reactions were also investigated in detail (Fig. 6(b)). Under open-circuit conditions (*i.e.*, before voltage application, black line in Fig. 6(b)), intense red emission bands were observed for Eu(hfa)$_3$(TPPO)$_2$ under excitation at 337 nm, representing the 'emission-on' state (photo in Fig. 6(b)). This red emission was completely quenched when a bias voltage of −2.0 V was applied (red line), resulting in an 'emission-off' state, and the emission intensity decreased to 99.3%.

Furthermore, the emission intensity and emission lifetime of the STN/Eu(hfa)$_3$(TPPO)$_2$ without HV^{2+} in the 2-electrode device were not influenced by the bias voltage (Fig. 7 and Fig. 8(a)), In contrast, the emission lifetime of the Eu(hfa)$_3$(TPPO)$_2$ complex in the STN/HV^{2+}/Eu(hfa)$_3$(TPPO)$_2$-based device decreased after the application of bias voltage (Fig. 8(b)), strongly indicating that the colored $HV^{\bullet+}$ species controlled the emission properties of Eu(hfa)$_3$(TPPO)$_2$. These findings demonstrate that efficient luminescence control is possible when EC materials and luminescent materials are present in the STN matrix.

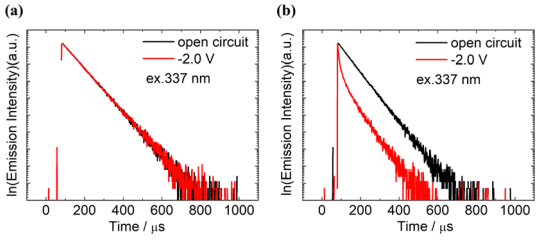

Fig. 8 Emission decay curves at 615nm ($^5D_0 \rightarrow {}^7F_2$) under open circuit condition (black line), and after the application of a bias voltage of −2.0 V for 150 s (red line). (a) STN/Eu(hfa)$_3$(TPPO)$_2$ device and (b) STN/HV^{2+}/Eu(hfa)$_3$(TPPO)$_2$ device.

3.4 Mechanism of the luminescence control in the EFC device

To discuss the mechanism of luminescence modulation, the photophysical properties of the EFC device comprising a modified ITO electrode with STN/HV^{2+}/Eu(hfa)$_3$(TPPO)$_2$ as the working electrode were investigated in detail. As shown in Fig. 9, the absorption band of the reduced species of $HV^{\bullet+}$ appears at approximately 600 nm, and it overlaps well with the emission bands of Eu(hfa)$_3$(TPPO)$_2$. This overlap enables efficient fluorescence resonance energy transfer (FRET) from the excited states of the Eu(III) complex to the ground states of the $HV^{\bullet+}$ molecules.[62–64] The photoinduced electron transfer may occur from the reduced state of $HV^{\bullet+}$ to the excited Eu(hfa)$_3$(TPPO)$_2$, leading to the formation of the reduced state of the Eu(hfa)$_3$(TPPO)$_2$ and resulting in luminescence quenching. In our previous report, we investigated the possibility of these kinds of photoinduced electron transfer between the Eu(III) complex and viologen derivatives. The results showed that the absorbance of the reduced state of $HV^{\bullet+}$ was not affected by the excitation of the Eu(III) complex.[27,65] In addition, the overlap of molecular orbital between the inner 4f electron orbital in the Eu^{3+} ions and the molecular orbital in viologen are suggested to be very small, which would reduce the extent of electron transfer.[62] These results indicate that electron transfer from reduced state of $HV^{\bullet+}$ to the excited Eu(hfa)^3(TPPO)^2 is not the main reason for the quenching process.

Photophysical parameters based on the emission spectra (Fig. 6(b)) were estimated using the LUMPAC software.[66] The I_{rel} value ($I_{rel} = I_{ED}/I_{MD}$) is used to indicate the sit symmetry of Eu^{3+},[67] and the luminescence quantum efficiency of the excited state of the Eu^{3+} ion (Φ_{Ln}) is defined as $k_r/(k_r + k_{nr})$.[68] As shown in Table 1, I_{rel} remained constant (13.05), indicating that the symmetrical structure of Eu(hfa)$_3$(TPPO)$_2$ did not change upon applying a voltage. Therefore, the k_r value was not influenced by the voltage application. On the other hand, the drastic increase

Table 1 Radiative transition rate (k_r), non-radiative transition rate (k_{nr}), symmetry factor (I_{rel}), intrinsic quantum efficiency (Φ_{Ln}), and emission lifetimes (τ_{ave}) of the STN/HV^{2+}/$Eu(hfa)_3(TPPO)_2$ device before and after voltage application

	k_r (s^{-1})	k_{nr} (s^{-1})	Φ_{Ln} (%)	I_{rel}	τ_{ave}(ms)
Open circuit	769	696	52.5	13.05	0.682
−2 V/150 s	769	1911	28.7	13.05	0.373

in the k_{nr} value and the decrease in Φ_{Ln} after applying voltage further indicate that the excited energy can be easily transferred from the excited state of the $Eu(hfa)_3(TPPO)_2$ to the colored $HV^{\bullet+}$ species *via* a non-radiative process. The energy transfer efficiency can be calculated using eqn (2).

$$E = 1 - \frac{\tau}{\tau_0} \quad (2)$$

where E is the energy transfer efficiency from the Eu(III) complex to colored $HV^{\bullet+}$, and τ_0 and τ are the luminescence lifetimes before and after applying the voltage, respectively. The luminescence lifetimes were calculated from Fig. 8(b) and are listed in Table 1; the energy transfer efficiency was calculated to be 45.3% using eqn (2). However, the red luminescence of $Eu(hfa)_3(TPPO)_2$ was almost completely quenched (99.3%) owing the EC reaction of HV^{2+} (Fig. 6(b)). This discrepancy is possibly because of the colored $HV^{\bullet+}$ molecules directly absorbing the luminescence from the Eu(III) complex without energy transfer, which is known as the inner filter effect,[69,70] this is another reason for the reduction in the emission intensity.

For the STN/HV^{2+}/$Eu(hfa)_3(TPPO)_2$-based device, the energy transfer pathways within the clay matrix were investigated by calculating the emission lifetime (τ), while the contribution (%) of each exponential component (τ_1, τ_2, and τ_3) was calculated from Fig. 8. These results are presented in Table 2. Before the application of voltage, the emission lifetime of the device exhibited only one exponential component (682 μs). After the application of voltage, the device exhibited a multi-exponential emission decay with three components: τ_1, τ_2, and τ_3, with contributions of 24%, 36%, and 40%, respectively. The value of the longer lifetime τ_3 component (τ_3; 682 μs) was same as that of the single component before applying voltage, indicating that it does not transfer energy to the colored $HV^{\bullet+}$ species. The shorter lifetime components (τ_1 and τ_2) component can be considered as components of the energy transferred to the colored $HV^{\bullet+}$ species. Using eqn (2), the energy transfer efficiency for the luminescence components of τ_1, τ_2 and τ_3 was calculated to be 92%, 65%, and 0, respectively. The total energy transfer from the τ_1, τ_2 and τ_3 components of the $Eu(hfa)_3(TPPO)_2$ complex to the colored $HV^{\bullet+}$ species was determined to be 45.5% (0.24 × 0.92 + 0.36 × 0.65 + 0.40 × 0), which is consistent with the value (45.3%) obtained from eqn (2), using the averaged luminescence lifetime (τ_{ave}).

Table 2 Emission lifetimes (τ), contribution (%) of the components, energy transfer efficiency (E), and donor–acceptor distance (r_{DA}) of STN/HV^{2+}/$Eu(hfa)_3(TPPO)_2$-based device before and after applying voltage

		τ_1(μs)	τ_2(μs)	τ_3(μs)
Open circuit	Emission lifetime	—	—	682
	Contribution (%)	—	—	100
−2.0 V/150 s	Emission lifetime	52	242	682
	Contribution (%)	24	36	40
	E (%)	92	65	0
	r_{DA} (nm)	4.75	6.44	—

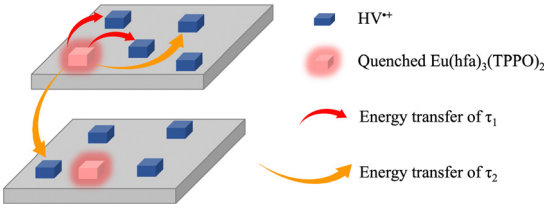

Fig. 10 Schematic diagram of energy transfer between $HV^{\bullet+}$ and $Eu(hfa)_3(TPPO)_2$ between STN layers.

Furthermore, the donor–acceptor distance (r_{DA}), the overlap integral J, and Förster distance (R_0) were calculated using the equations provided in the ESI.† As shown in Table 2, the donor–acceptor distance (r_{DA}) for the τ_1 component is 4.75 nm, while that for the τ_2 component is 6.44 nm. The average inter-anionic charge distance on the clay surface was approximately 1.2 nm.[71] However, the actual intermolecular distances within the clay layer depend on the molecular size. Furthermore, steric and electrostatic repulsions between the adsorbed molecules may enlarge intermolecular distances.[72] In the interlayers of the STN matrix, 50% of the methyltri-*n*-octylammonium ions remained unexchanged, leading to an increased donor–acceptor distance. Consequently, there are two positional pathways for the energy transfer between the colored $HV^{\bullet+}$ species and the $Eu(hfa)_3(TPPO)_2$ complex. Fig. 10 shows a schematic of the proposed energy transfer process in the STN/HV^{2+}/$Eu(hfa)_3(TPPO)_2$-based device. For the τ_1 component, the energy transfer was as high as 92%, primarily occurring within the same STN layer, from the $Eu(hfa)_3(TPPO)_2$ complex to the adjacent colored $HV^{\bullet+}$ species. In the case of the τ_2 component, the r_{DA} was estimated to be 6.44 nm which is significantly larger than the thickness of an STN layer (1 nm). The energy transfer efficiency for the τ_2 component was lower value (65%). This energy transfer is considered to occur both within the same STN layer with a longer molecular distance, and *via* vertical energy transfer between different STN layers.

4 Conclusions

In this study, we have developed an electro-switchable emission and coloration device by incorporating the luminescent $Eu(hfa)_3(TPPO)_2$ complex, and the electrochromic HV^{2+} molecule into a synthesized smectite (STN) matrix. The adsorption capacities of different molecules on STN were studied, and it was found that approximately 80% of HV^{2+} and 20% of $Eu(hfa)_3(TPPO)_2$ were adsorbed onto the STN in the case with a 25% : 16.7% *vs.* CEC ratio. The electrochemical properties of HV^{2+} and $Eu(hfa)_3(TPPO)_2$ in the STN matrix were also investigated. The results indicated that $Eu(hfa)_3(TPPO)_2$ expanded the

interlayer spacing of the STN, thereby facilitating movement of electrolyte and consequently enhancing the electrochromic properties of HV^{2+}. The red photoluminescence of $Eu(hfa)_3(TPPO)_2$ was clearly observed under open circuit conditions. The electrochemically colored $HV^{\bullet+}$ species (cyan color) efficiently quenched the red emission of the $Eu(hfa)_3(TPPO)_2$ by the application of a bias voltage of −2.0 V for 150 s. The emission color change of the device was achieved *via* both energy transfer from the excited state of $Eu(hfa)_3(TPPO)_2$ to the colored $HV^{\bullet+}$ state and reabsorption of the luminescence from the $Eu(hfa)_3(TPPO)_2$ complex by the colored $HV^{\bullet+}$ species, thereby resulting in a device with dual emissive and reflective modes *via* electrochemical reactions. We believe that this dual-mode device will contribute significantly to the development of sensors and display devices.

Author contributions

Rong Cao: review, editing, writing original draft, formal analysis, funding acquisition, and supervision. Naoto Kobayashi: validation, data curation, and investigation. Kazuki Nakamura: editing, methodology, and funding acquisition. Norihisa Kobayashi: funding acquisition, supervision, and resources.

Data availability

All data for this study are available in this main text or are included in the ESI.†

Conflicts of interest

There are no conflicts to declare.

Acknowledgements

This work was partly supported by JSPS KAKENHI (17H06377, 20K05641, and 23K04871), the New Energy and Industrial Technology Development Organization (JPNP20004), the Izumi Science and Technology Foundation, and the Iketani Science and Technology Foundation. This work was also supported by JST SPRING, Grant Number JPMJSP2109.

References

1 L. Hu, Q. Zhang, X. Li and M. J. Serpe, *Mater. Horiz.*, 2019, **6**, 1774–1793.
2 Y. S. Lui, W. T. Sow, L. P. Tan, Y. Wu, Y. Lai and H. Li, *Acta Biomater.*, 2019, **92**, 19–36.
3 A. P. de Silva and N. D. McClenaghan, *Chem. – Eur. J.*, 2004, **10**, 574–586.
4 M. Irie, *Chem. Rev.*, 2000, **100**, 1685–1716.
5 Y. Watanabe, K. Nakamura and N. Kobayashi, *Chem. Lett.*, 2010, **39**, 1309–1311.
6 K. Ogasawara, K. Nakamura and N. Kobayashi, *J. Mater. Chem. C*, 2016, **4**, 4805–4813.
7 S. Hirata, K.-S. Lee and T. Watanabe, *Adv. Funct. Mater.*, 2008, **18**, 2869–2879.
8 Y. Kitagawa, M. Kumagai, P. P. Ferreira da Rosa, K. Fushimi and Y. Hasegawa, *Chem. – Eur. J.*, 2021, **27**, 264–269.
9 J. Chen, Z. Xie, L. Meng, Z. Hu, X. Kuang, Y. Xie and C.-Z. Lu, *Inorg. Chem.*, 2020, **59**, 6963–6977.
10 M. Irie, T. Fukaminato, T. Sasaki, N. Tamai and T. Kawai, *Nature*, 2002, **420**, 759–760.
11 L. Jia, B. Zhang, J. Xu, T. Zhu, R. Chen and F. Zhou, *ACS Appl. Mater. Interfaces*, 2020, **12**, 19955–19964.
12 S. Shinoda and H. Tsukube, *Analyst*, 2011, **136**, 431–435.
13 T. Sagami, Y. O. Tahara, M. Miyata, H. Miyake and S. Shinoda, *Chem. Commun.*, 2017, **53**, 3967–3970.
14 P. R. Somani and S. Radhakrishnan, *Mater. Chem. Phys.*, 2003, **77**, 117–133.
15 C. Gu, A.-B. Jia, Y.-M. Zhang and S. X.-A. Zhang, *Chem. Rev.*, 2022, **122**, 14679–14721.
16 S. Kimura, T. Sugita, K. Nakamura and N. Kobayashi, *Nanoscale*, 2020, **12**, 23975–23983.
17 A. Tsuboi, K. Nakamura and N. Kobayashi, *Adv. Mater.*, 2013, **25**, 3197–3201.
18 C. G. Granqvist, *Thin Solid Films*, 2014, **564**, 1–38.
19 C.-Y. Hsu, J. Zhang, T. Sato, S. Moriyama and M. Higuchi, *ACS Appl. Mater. Interfaces*, 2015, **7**, 18266–18272.
20 P. Tehrani, L.-O. Hennerdal, A. L. Dyer, J. R. Reynolds and M. Berggren, *J. Mater. Chem.*, 2009, **19**, 1799–1802.
21 M. Chang, W. Chen, H. Xue, D. Liang, X. Lu and G. Zhou, *J. Mater. Chem. C*, 2020, **8**, 16129–16142.
22 Y. Kim, H. Ohmagari, A. Saso, N. Tamaoki and M. Hasegawa, *ACS Appl. Mater. Interfaces*, 2020, **12**, 46390–46396.
23 H. Al-Kutubi, H. R. Zafarani, L. Rassaei and K. Mathwig, *Eur. Polym. J.*, 2016, **83**, 478–498.
24 M. Tropiano, N. L. Kilah, M. Morten, H. Rahman, J. J. Davis, P. D. Beer and S. Faulkner, *J. Am. Chem. Soc.*, 2011, **133**, 11847–11849.
25 S. Mondal, D. C. Santra, S. Roy, Y. S. L. V. Narayana, T. Yoshida, Y. Ninomiya and M. Higuchi, *ACS Appl. Mater. Interfaces*, 2023, **15**, 42912–42919.
26 K. Nakamura, K. Kanazawa and N. Kobayashi, *Chem. Commun.*, 2011, **47**, 10064–10066.
27 K. Nakamura, K. Kanazawa and N. Kobayashi, *Displays*, 2013, **34**, 389–395.
28 N. Sun, Z. Zhou, D. Chao, X. Chu, Y. Du, X. Zhao, D. Wang and C. Chen, *J. Polym. Sci., Part A:Polym. Chem.*, 2017, **55**, 213–222.
29 T. Fu, Y.-L. Wei, C. Zhang, L.-K. Li, X.-F. Liu, H.-Y. Li and S.-Q. Zang, *Chem. Commun.*, 2020, **56**, 13093–13096.
30 K. Kanazawa, K. Nakamura and N. Kobayashi, *Sol. Energy Mater. Sol. Cells*, 2016, **145**, 42–53.
31 C. L. Bird and A. T. Kuhn, *Chem. Soc. Rev.*, 1981, **10**, 49–82.
32 Y. Hirai, T. Nakanishi, Y. Kitagawa, K. Fushimi, T. Seki, H. Ito, H. Fueno, K. Tanaka, T. Satoh and Y. Hasegawa, *Inorg. Chem.*, 2015, **54**, 4364–4370.
33 A.-S. Chauvin, S. Comby, B. Song, C. D. B. Vandevyver and J.-C. G. Bünzli, *Chem. – Eur. J.*, 2008, **14**, 1726–1739.

34 B. Song, G. Wang, M. Tan and J. Yuan, *J. Am. Chem. Soc.*, 2006, **128**, 13442–13450.
35 J.-C. G. Bünzli, *Chem. Rev.*, 2010, **110**, 2729–2755.
36 Y. Hasegawa and Y. Kitagawa, *J. Photochem. Photobiol., C*, 2022, **51**, 100485.
37 A. Walcarius, S. D. Minteer, J. Wang, Y. Lin and A. Merkoçi, *J. Mater. Chem. B*, 2013, **1**, 4878–4908.
38 K. Okamoto, S. Sinha Ray and M. Okamoto, *J. Polym. Sci., Part B: Polym. Phys.*, 2003, **41**, 3160–3172.
39 R. A. Vaia and E. P. Giannelis, *Macromolecules*, 1997, **30**, 7990–7999.
40 M. Alexandre and P. Dubois, *Mater. Sci. Eng., R*, 2000, **28**, 1–63.
41 T. Fujimura, T. Shimada, R. Sasai and S. Takagi, *Langmuir*, 2018, **34**, 3572–3577.
42 L. Zhang, W.-B. Zhang, S.-S. Chai, X.-W. Han, Q. Zhang, X. Bao, Y.-W. Guo, X.-L. Zhang, X. Zhou, S.-B. Guo and X.-J. Ma, *J. Electrochem. Soc.*, 2021, **168**, 070558.
43 C. Mousty, *Appl. Clay Sci.*, 2004, **27**, 159–177.
44 M.-S. Chen, W. Fu, Y. Hu, M.-Y. Chen, Y.-J. Chiou, H.-M. Lin, M. Zhang and Z. Shen, *Nanoscale*, 2020, **12**, 16262–16269.
45 H. Li, M. Li, Y. Wang and W. Zhang, *Chem. – Eur. J.*, 2014, **20**, 10392–10396.
46 S.-J. Ryu, A. Kim, M. D. Kim, S. W. Hong, S. S. Min, J.-H. Lee, J.-K. Lee and H. Jung, *Appl. Clay Sci.*, 2014, **101**, 52–59.
47 Y. Wang, P. Li, S. Wang and H. Li, *J. Rare Earths*, 2019, **37**, 451–467.
48 K. Nakamura, N. Yanagawa and N. Kobayashi, *Materials*, 2022, **15**, 5202.
49 T. Fujimura, T. Shimada, S. Hamatani, S. Onodera, R. Sasai, H. Inoue and S. Takagi, *Langmuir*, 2013, **29**, 5060–5065.
50 D. Janeba, P. Čapková, Z. Weiss and H. Schenk, *Clays Clay Miner.*, 1998, **46**, 63–68.
51 Z. Klapyta, T. Fujita and N. Iyi, *Appl. Clay Sci.*, 2001, **19**, 5–10.
52 Y. Hasegawa, M. Yamamuro, Y. Wada, N. Kanehisa, Y. Kai and S. Yanagida, *J. Phys. Chem. A*, 2003, **107**, 1697–1702.
53 P. Boháč, Š. Budzák, V. Planetová, R. Klement and J. Bujdák, *J. Phys. Chem. C*, 2022, **126**, 17255–17265.
54 S. R. Valandro, A. L. Poli, T. F. A. Correia, P. C. Lombardo and C. C. Schmitt, *Langmuir*, 2017, **33**, 891–899.
55 Z. Li, K. Nakamura and N. Kobayashi, *J. Mater. Chem. C*, 2023, **11**, 118–126.
56 K. Nakamura, H. Minami, A. Sagara, N. Itamoto and N. Kobayashi, *J. Mater. Chem. C*, 2018, **6**, 4516–4522.
57 Y.-Y. Wang, L. Song, S.-Y. Tang, Z.-Q. Dai, J.-Y. Guo, H.-Y. Shen and W.-X. Chai, *Mater. Today Commun.*, 2022, **32**, 104054.
58 Y.-Y. Wang, L. Song, J.-T. Wang, Y.-M. Zhou, Z.-Q. Dai, W. Liu, J.-Y. Guo, H.-Y. Shen and W.-X. Chai, *Appl. Organomet. Chem.*, 2022, **36**, e6752.
59 R. Ilmi, D. Zhang, L. Tensi, H. Al-Sharji, N. K. Al Rasbi, A. Macchioni, L. Zhou, W.-Y. Wong, P. R. Raithby and M. S. Khan, *Dyes Pigm.*, 2022, **203**, 110300.
60 R. J. Mortimer and J. R. Reynolds, *Displays*, 2008, **29**, 424–431.
61 M. Eguchi, M. Momotake, F. Inoue, T. Oshima, K. Maeda and M. Higuchi, *ACS Appl. Mater. Interfaces*, 2017, **9**, 35498–35503.
62 K. Kanazawa, Y. Komiya, K. Nakamura and N. Kobayashi, *Phys. Chem. Chem. Phys.*, 2017, **19**, 16979–16988.
63 K. Nakamura, N. Yanagawa and N. Kobayashi, *J. Soc. Inf. Disp.*, 2022, **30**, 15–23.
64 T. Fujimura, T. Shimada, R. Sasai and S. Takagi, *Clays Clay Miner.*, 2019, **67**, 537–544.
65 K. Kanazawa, K. Nakamura and N. Kobayashi, *ChemistrySelect*, 2018, **3**, 9672–9680.
66 J. D. L. Dutra, T. D. Bispo and R. O. Freire, *J. Comput. Chem.*, 2014, **35**, 772–775.
67 P. A. Tanner, *Chem. Soc. Rev.*, 2013, **42**, 5090–5101.
68 H. Minami, M. Miyazato, Z. Li, K. Nakamura and N. Kobayashi, *Chem. Commun.*, 2020, **56**, 13532–13535.
69 X.-F. Yang, P. Liu, L. Wang and M. Zhao, *J. Fluoresc.*, 2008, **18**, 453–459.
70 P. P. Pompa, G. Ciccarella, J. Spadavecchia, R. Cingolani, G. Vasapollo and R. Rinaldi, *J. Photochem. Photobiol., A*, 2004, **163**, 113–120.
71 Y. Ishida, *Bull. Chem. Soc. Jpn.*, 2021, **94**, 2886–2897.
72 S. Takagi, T. Shimada, Y. Ishida, T. Fujimura, D. Masui, H. Tachibana, M. Eguchi and H. Inoue, *Langmuir*, 2013, **29**, 2108–2119.